HENRY GRANJON PRIZE COMPETITION 2007
Winner, Category B
"Materials behaviour and weldability"

DEVELOPMENT OF A COMPRESSIVE RESIDUAL STRESS FIELD AROUND A WELD TOE BY MEANS OF PHASE TRANSFORMATIONS

F. Martinez Díez

**Center for Welding, Joining and Coatings Research,
Colorado School of Mines-Golden CO (United States)**

ABSTRACT

Mechanically- or thermally-induced compressive stress fields have been used for decades to increase the fatigue performance of welded joints. By means of partial stabilization of austenite in the weld metal and subsequent controlled decomposition into martensite, a compressive residual stress field can be induced at the weld toe without the need of post weld processing. By proper adjustment of manganese and chromium content, a weld metal that produces a martensitic microstructure has been developed. This alloy begins its austenite-to-martensite transformation at a temperature below that at which the thermal contraction effects can negate the phase-induced volumetric expansion. The transformation also ends above room temperature to ensure the maximum volumetric expansion. Silicon additions to the manganese-chromium alloy produced welds with large weld toe radii of curvature.

IIW-Thesaurus keywords: *Arc welding; Fatigue improvement; Gas shielded arc welding; Martensite; Reference lists; Residual stresses; Steel construction; Transformation.*

1 INTRODUCTION

Today's highly competitive industrial environment requires higher standards of service life in welded structures. Improved design, manufacturing, and inspection methodologies have increased the service life of welded components, effectively shifting the areas of concern away from the welded joints. Still, up to 14 percent of all engineering component failures can be related to fatigue [1]. As such, fatigue control remains as one of the most important concerns in the welding industry.

The thermal contraction that all welds undergo during cooling to room temperature typically results in tensile stresses in the vicinity of the welded joint. The residual stress is caused by dissimilar volumetric contraction around the weld due to slight differences in the local peak temperature. To make things even more complex, a weld joint represents a discontinuity in geometrical and mechanical properties. That is, the continuity of stress is modified by the presence of welds, which act as stress concentrators. The stress concentration, in addition to the tensile residual stresses, always results

Doc. IIW-1891-08 (ex-doc. IX-2231r1-07) recommended for publication by Commission IX "Behaviour of metals subjected to welding".

in lower fatigue life for a welded joint when compared with the base material.

Several techniques to minimize or eliminate the tensile residual stress, or even induce compressive residual stress fields have been developed in the last decades. Unfortunately, these techniques require post-weld processing of the welded component.

Other methods that increase the fatigue performance of welded joints without requiring post-weld processing have been developed in the last few years. These methods are based on the relative unit cell size differences between body centred tetragonal (BCT) and face centred cubic (FCC) phases of steel. In the constraint of solid state, the formation of martensite and subsequent volume increase of the unit cell will induce a compressive residual stress in the region surrounding the transformed material. The resulting compressive stress state has been shown to increase the fatigue limit of plain-carbon steel structural welds by as much as three times that of conventional weld metals [2, 3].

This research focussed upon quantifying the influence of manganese, nickel and chromium additions on the development of a martensitic microstructure in structural steel weld metals. Metal-cored wires with varied compositions were manufactured for this study. The results were used to develop a low cost weld alloy that would induce maximum compressive residual stress at the weld toe. The designed welding alloy was intended for joining low-carbon, high-strength steels.

In the development of these weld metals, models to help understand the martensitic phase evolution within the compositional limits of this study were developed. Based upon equivalent ratios of ferrite to austenite stabilizers, a boundary between primary ferritic and austenitic weld metals was devised. The relative effects of chromium, nickel, and manganese on the martensite start (M_S) and finish (M_F) temperatures were quantified and compared with predictions. Discrepancies between calculated and measured transformation temperatures were explained with the developed primary phase models. This work describes the progress achieved in the development of transformation-induced compressive residual stresses.

2 EXPERIMENTAL PROCEDURE

The experimental approach involved the practical understanding of the effects of chromium, nickel, and manganese additions on the martensite formation. Experimental metal-cored welding wires of 1.3 mm diameter were manufactured, cleaned with acetone, baked at 160 °C for six hours to remove moisture, and stored in a controlled environment. The composition of these wires is shown in Table 1. As seen in Figure 1, these compositions spanned across the entire complete-martensite field of the Schaeffler diagram.

Chromium content was set at 10 weight percent since previous studies [2, 3] presented it as the required content to balance the austenite stabilizing additions (Mn & Ni) to produce a weld metal that would induce a compressive residual stress by means of martensitic transformation. Manganese was added as ferro-manganese while nickel was used in its pure form. The rest of the alloying elements came as part of the stainless-steel strip (low carbon AISI 409) used for the manufacturing of these wires.

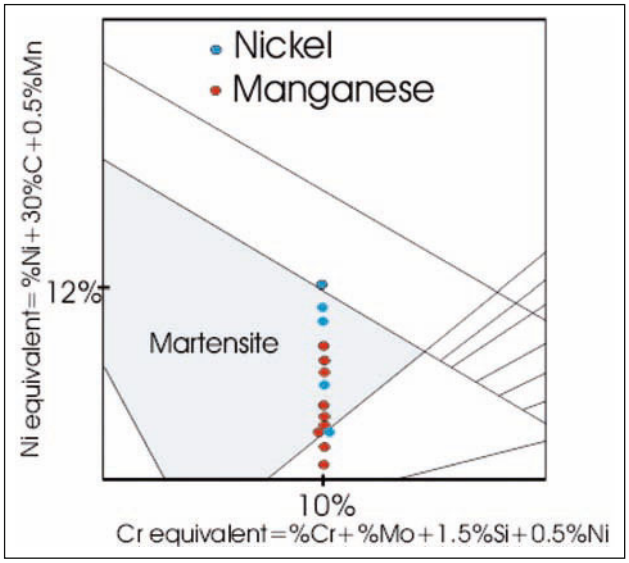

Figure 1 – Portion of the Schaeffler diagram depicting the experimental matrix of this study

To eliminate the potential threshold due to weld metal dilution on the results of this study, all but the final studies (residual-stress measurement) were done on non-diluted samples. These samples were produced by fusing the GMAW-MC wires on a water-chilled copper mold. Copper contamination was never found in any of the analyzed samples.

Table 1 – Composition of experimental weld metals and transformation temperatures (LECO SA-2000 Glow Discharge Sputtering Spectrometer)

Wire code	wt. % content*			
	Cr	Mn	Ni	Si
Mn1	12.30	1.80	0.10	0.31
Mn2	11.80	3.70	0.10	0.28
Mn3	11.20	5.90	0.10	0.29
Mn4	11.30	7.60	0.10	0.33
Mn5	10.80	9.00	0.10	0.27
Mn6	11.20	12.80	0.10	0.30
Mn7	10.70	14.40	0.10	0.28
Cr1	10.50	0.10	0.10	0.31
Ni1	11.00	0.20	3.40	0.31
Ni2	11.30	0.20	6.20	0.28
Ni3	12.00	0.20	10.00	0.29
Ni4	9.80	0.20	11.20	0.31
Ni5	10.40	0.20	12.20	0.30
Si1	10.00	8.50	0.10	0.28
Si2	9.80	6.20	0.10	0.57
Si3	10.00	8.50	0.10	1.88
Si4	9.90	10.70	0.10	0.67
Si5	9.80	5.90	0.10	0.41

*C = 0.04 wt. %, < 0.2 wt. % residuals, balance Fe.

2.1 Dilatometric analyses

The compositions in Table 1 were deposited (32 V, 4.3 mm/s, 90Ar10O_2 at 21 L/min, 300-350 A) to produce all-weld metal nuggets, each consisting of three to four beads. The samples were later machined to cylindrical and squared shape rods with a cross-sectional area between 9 and 25 square millimetres. The length of these specimens varied between 15 and 20 millimetres. The variance in the size of the samples was due to geometrical variance of the original weld nuggets. Elemental additions, especially those of manganese, tended to reduce the fluidity of the molten metal, resulting in irregular-shaped weld nuggets. The effect of the geometric differences was eliminated by using normalized sizes in the analyses.

With the aid of a Gleeble 1500 Thermomechanical Simulator, non-diluted weld metal samples were subjected to a thermal cycle that simulated the cooling cycle austenite undergoes after welding (see Figure 2). The inflexion points in the circumferential dilatation (strain) recorded during the cooling stage (helium blast) were taken as the M_S and M_F temperatures.

2.2 Segregation analyses

Segregation analyses were conducted on selected samples by means of energy dispersive spectroscopy (EDS). Samples obtained by quenching of non-diluted weld nuggets as well as dilatometric samples were examined.

Both transverse and longitudinal sections of the weld samples were examined with a 20 kV and 0.25 μA beam of less than a micrometer diameter. A resolution of two micrometers was achieved with this methodology. All analyses consisted of 5 000 counts per every 10 micrometres of the analyzed section.

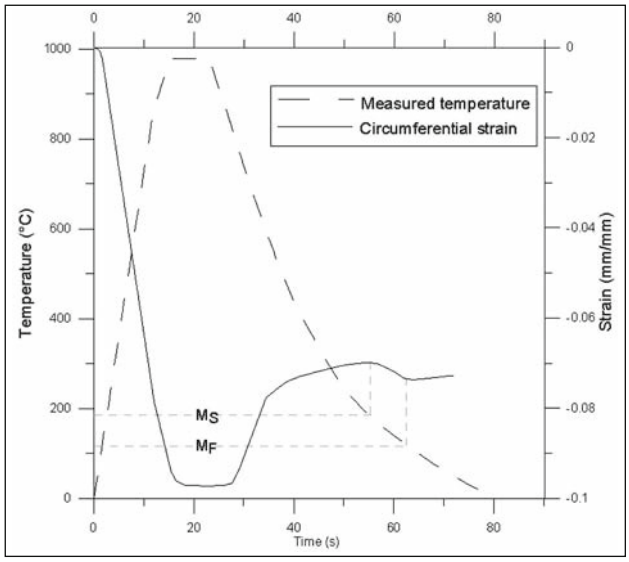

Figure 2 – Typical (Ni3 alloy) temperature vs. time and stain vs. time profile As evaluated with circumferential dilatometers (Gleeble 1500)

Figure 3 shows an EDS scan from one dendrite tip (A) to another (D) across the interdendritic region (BC).

2.3 Metallographic analyses

A methodology based initially on metallographic analyses and then X-ray diffraction was used to evaluate the primary solidification phase. A grain boundary etchant based on the one developed by Hultgren [4] was used to reveal the solidification grain boundaries, and to determine the first phase that forms based on the solidification mode.

When the etchant to develop primary solidification structure (PSS) (Table 2) was applied (10 to 15 seconds

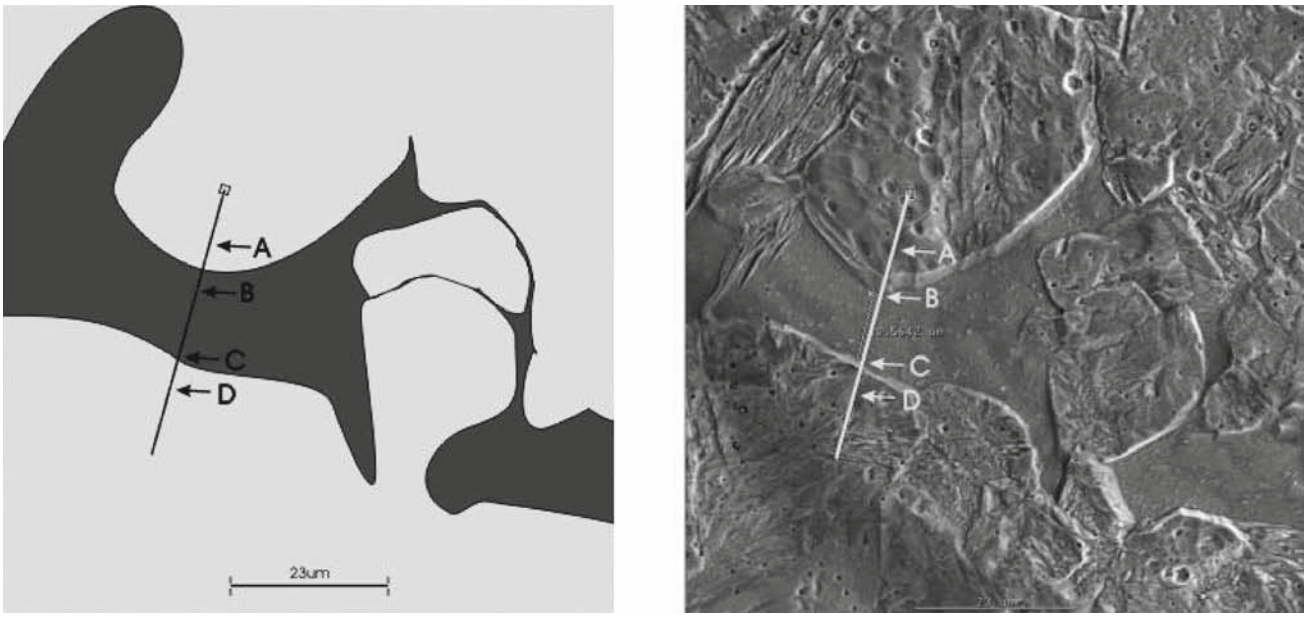

a) Schematic representation **b) Electron micrograph**

In both sections points A and D correspond to two different dendrite arms, B and C to the dendrite solidification boundary and the line to the actual analyzed section.

Figure 3 – Typical EDS linear analysis

Table 2 – Primary Solidification Structure (PSS) etchant

2.5 g	$FeCl_3$
2.5 g	$CuCl_2$
50 ml	HCl
150 ml	H_2O
40 ml	C_2H_5OH

immersion) on samples that were diamond-polished to 0.25 micrometer, the primary solidification structure was revealed. After prolonged etching, the secondary solid-state transformation structure would be developed with the disappearance of the primary solidification structure.

A simple solution based on nitric and hydrochloric acids (Table 3) was used to develop the final transformation microstructures. This etchant revealed the austenite/martensite (A/M) component as a mixture of fine dark features (Figure 4). Differentiation of martensite from austenite by optical means proved to be a difficult and inaccurate task; therefore, X-ray diffraction was used for their quantification (see next section). On the other hand, retained ferrite could be easily identified as a white and irregular feature. Precipitates of all kinds could also be revealed with this etchant as round dark features.

2.4 X-Ray diffraction analyses

X-ray diffraction analyses (45 kV, 40 mA Cu radiation, eight peaks monitoring) were performed to identify phases and map their evolution. All specimens used in this analysis were either quenched metallographic or dilatometric samples. They were all prepared by grinding with 500 grit and very little pressure to avoid the development of deformation-induced martensite.

Table 3 – Final transformation structure (martensite) etchant (FS etchant)

10 ml	H_2NO_3
20 ml	HCl
30 ml	H_2O

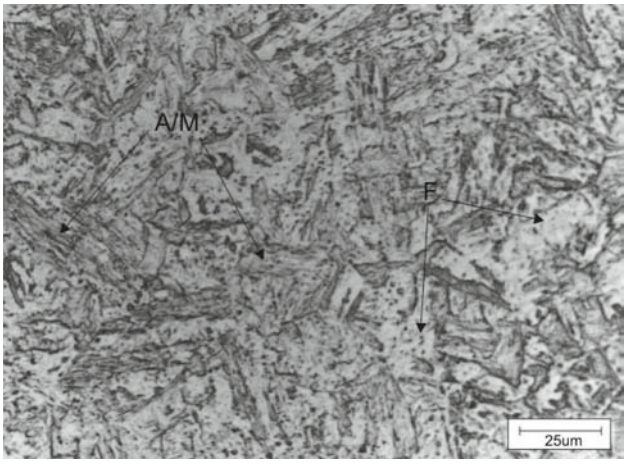

Figure 4 – Ni1 sampled etched to reveal the final microstructure – Martensite plus austenite

Due to the low carbon content in the alloys, the martensite in all samples displayed very little tetragonality, thus no difference in the diffraction angle between bcc and bct phases (i.e. peak splitting) could be resolved. Therefore, all recorded bcc/bct peaks were treated as a ferrite/martensite component and the final differentiation was done by means of metallographic analyses. With the computed intensities of the different diffraction peaks, the final volume quantification was given by the average of three criteria [5]: Cullity, Deshayes, and ASTM.

10 mm fillets (32 V, 4.3 mm/s, 300-350 A) on 12 mm thick EN 10137 plates (Quench and tempered high strength steel) were analyzed for residual stress. The magnitude and extent of the induced compressive residual stress field was quantified by means of X-ray diffraction measurements (90°, 67.5°, and 45° diffraction angle; five acquisitions, three diffraction peaks monitoring). This methodology resulted in a computed error of less than 25 MPa. Subsurface measurements were made by electrolytic removal of material so the stress field would not be distorted by plastic deformation.

3 RESULTS AND DISCUSSION

3.1 Preliminary phase-assessment

Hardness measurements of fused (non-diluted) samples revealed a compositional limit where the hardness suddenly dropped. Weld metals containing more than 10 wt. percent nickel exhibited a hardness that was 30 HRA points less than that of leaner alloys (see Figure 5).

Metallographic inspection of the high nickel samples revealed a final microstructure consisting of round features and some small precipitates (Figure 6). These spherical features did not resemble known martensite

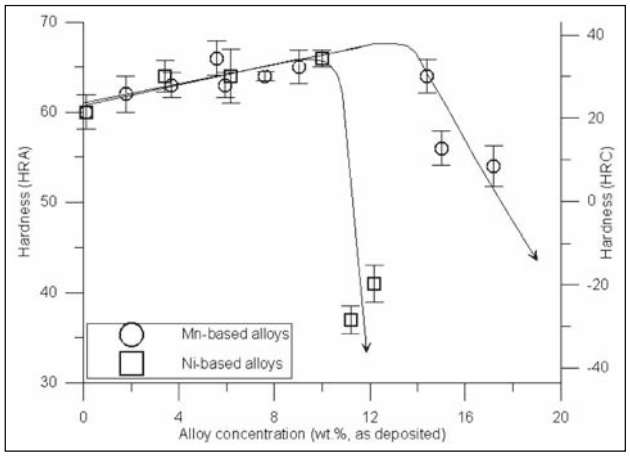

Detailed compositions are found in Table 1. Non-diluted samples.

Figure 5 – Hardness measurements for the Ni- and Mn- based weld metals

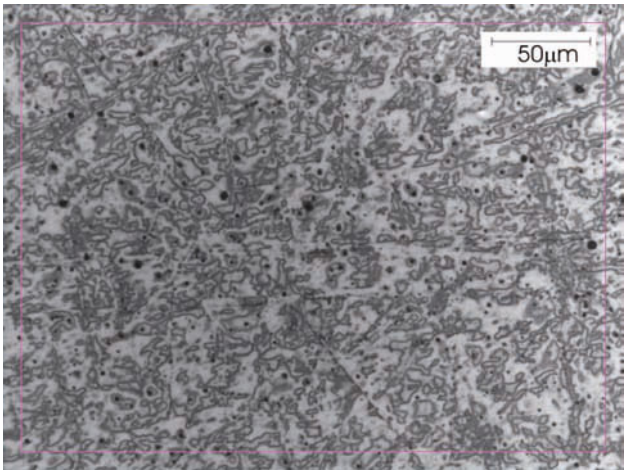

FS etchant (Table 3).

Figure 6 – Ni4 (10Cr-11Ni) composition cooled on air - Austenite

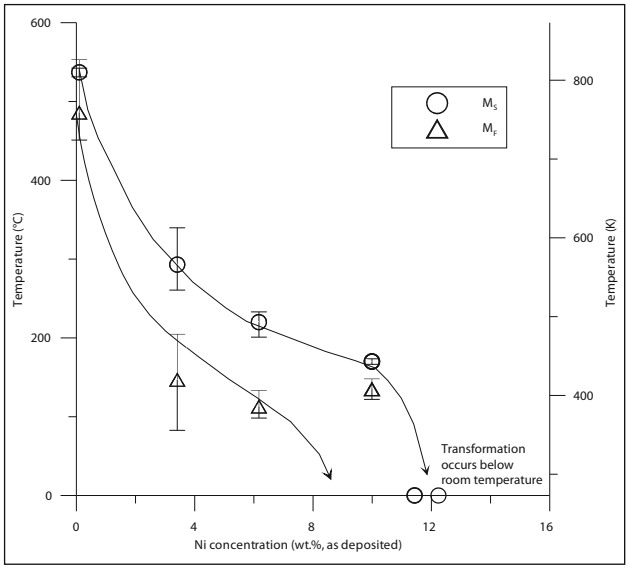

Figure 7 – Martensite transformation temperatures for the Ni-based weld metals – Gleeble 1500 Thermomechanical Simulator

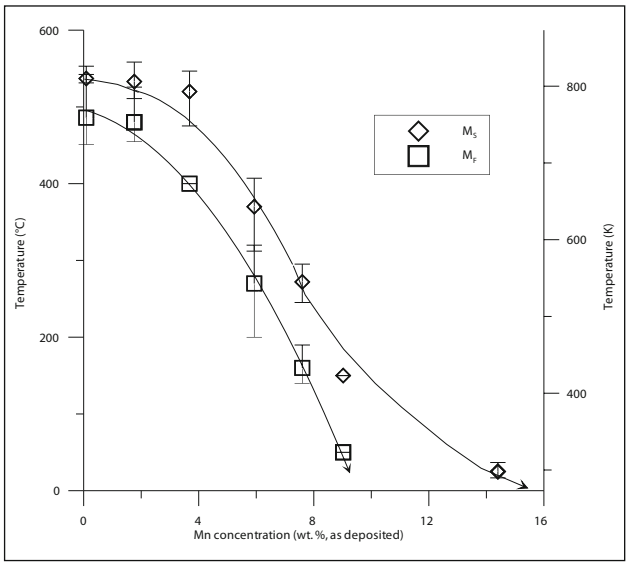

Figure 8 – Martensite transformation temperatures for the Mn-based weld metals – Gleeble 1500 Thermomechanical Simulator

microstructures. Although final microstructure models like the one developed by Schaeffler (Figure 1) predicted these high-alloy compositions to be martensite, their hardness level (40 HRA) did not correspond to the high hardness of this phase. After more in-depth analysis by means of XRD inspection, this microstructure was concluded to be austenite.

Manganese-based weld compositions exhibited a similar behaviour. Compositions above 14 weight percent manganese revealed a lower hardness than leaner alloys. Although the hardness decrease did not seem to be as radical as in the nickel case, metallographic analyses confirmed the absence of martensite.

This evidence defined a compositional limit for the martensitic transformation in both alloy systems. As the austenite stabilizer (Ni or Mn) content is increased, the stabilization of austenite down to room temperature should be expected. When austenite becomes more stable, the martensitic transformation is hindered and a lower hardness results.

From this phase assessment, a compositional limit was established: at 10 wt. % Cr, compositions over 10 wt. % nickel or 14 wt. % manganese resulted in austenite that was stable down to room temperature.

A weld alloy that would induce a maximum compressive residual stress at the weld toe would require a maximum martensite fraction. This compositional limit served as the maximum point for such compositional window.

3.2 The martensitic transformation

The compositional limits established in the previous section were confirmed with dilatometric analyses. Indeed, compositions over 10 weight percent nickel did not manifest any volumetric expansion. Leaner compositions were evaluated for both martensite start and finish temperatures. Results from this analysis are presented in Figure 7 for the case of Ni-based alloys and in Figure 8 for the case of Mn-based ones.

From the comparison of these last two figures, it can be observed that both sets of curves have a common origin at 0 weight percent alloy addition. The Cr1 composition (Table 1) is the common point for both trends. The different behaviour that these trends exhibit merely reflects the differences between nickel and manganese in stabilizing the austenite and promoting the martensite formation.

These trends should not be expected to be similar since the two elements are different in nature. Unequal size, electronic configuration, and crystal structure will result in variations in the relative effect they have on the austenite stabilization, and in consequence in modifying the martensite transformation temperatures.

Still, a common point should exist. At zero nickel or manganese, and with the other alloying contents similar,

a common set of transformation temperatures should exist. The Cr1 alloy serves as this common point and therefore serves to validate the trends presented.

Unfortunately, no agreement with predicted martensite start temperature values was found (Figure 9 and Figure 10). None of the equations [6, 7] could predict the experimentally measured martensite start temperatures. Differences in the experimental matrices from which those predictive equations derive and that from this study can explain the discrepancy of the measured values. Different alloying contents can result in differences in the primary solidification phase, which can modify the segregation level of the alloying elements. By modifying the concentration of shear-limiting atoms in solution, the thermodynamics of the martensitic transformation are altered. This difference in the equilibrium temperature (T_0) between γ (austenite) and martensite due to alloy segregation render most of the predictive models inadequate. None of the employed M_S predictive models accounts for the primary solidification phase and the resulting segregation differences [8].

Each of the M_S curves in Figure 7 and Figure 8 show inflexion points. In the nickel-based weld metals, there is a slight reduction of the slope around 6.5 weight percent and an abrupt slope change just above 10 weight percent (Figure 7). The significance of the first inflexion point will be discussed in greater detail in later sections of this document. The inflexion point occurring around 9.5 weight percent in the manganese trend (Figure 8) will be explained in parallel. Both inflexion points might have their origin in a modification of the segregation pattern.

The second inflexion point of the Ni-trend (10 wt. % Ni) is clearly related to the stabilization of austenite. This type of behaviour is not observable in the Mn-based trend since no dilatometric analyzes were conducted below room temperature. A change in the curvature of the trend should occur at temperatures below those analyzed. Based on the observation of the trend, it should occur just below zero degree Celsius at a composition over 16 weight percent.

3.3 Solidification of an alloy and the resulting segregation

A phase diagram can provide a first description of the elemental distribution of a solidified alloy. The liquidus and solidus surfaces will dictate the compositions of the first and last solids to form. When an alloy of composition C_0 starts to solidify under equilibrium conditions, the composition of the first solid would be that dictated by the solidus. Depending on the partitioning of the involved elements, this solid can be of higher or lower composition than the bulk of the alloy. Upon further solidification, the solid composition will shift to C_0, the composition of the last solid to form. However, this initial description must be modified to define the real compositional profile of weld metals.

Although the initial solidification composition is dependent upon the bulk alloy content, non-equilibrium solidification and solute rejection (typical of weldment solidification) can alter it. This results in some alloying elements being rejected to the remaining liquid and some others being depleted from it.

This shifting of compositions can also result in modifications to the phase stability in the primary solidification structure as well as in the last region to solidify. In otherwise primary ferritic alloys, higher concentration of austenite-stabilizer elements (Ni, Mn) or lower concentration of ferrite stabilizers (Cr, Si) can favour the formation of austenite during solidification. Similarly, a local increase of ferrite stabilizer elements in the first solid to form can favour the formation of δ-ferrite in austenitic stainless steels [9, 10].

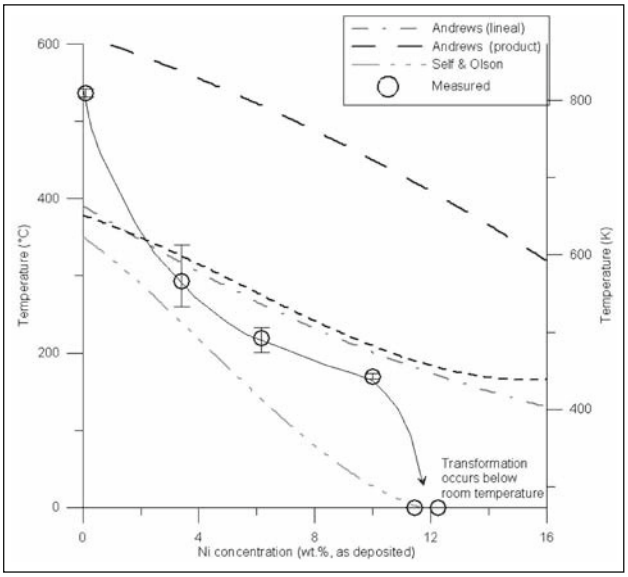

Figure 9 – Comparison of the analyzed martensite start temperatures of the Ni-based weld metals with predictive values

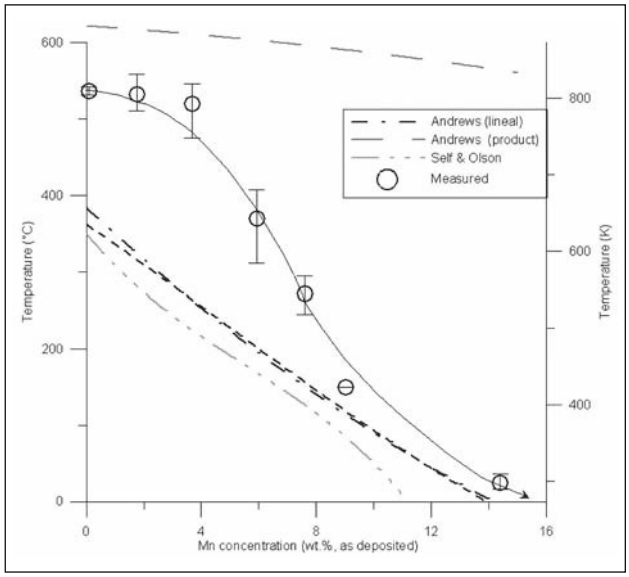

Figure 10 – Comparison of the analyzed martensite start temperatures of the Mn-based weld metals with predictive values

Because of the non-equilibrium nature of weldments' solidification, no complete mixing can occur in the liquid and solute redistribution plays a major role in controlling the solidification mode. The composition on either side of the solid-liquid interface is dictated by the partitioning coefficient (k). While it is true that Marangoni flows and electromagnetic fields can induce mechanical mixing in the molten pool, at the solid-liquid interface there is no mixing due to the stagnant boundary effect [9]. Diffusion times are too short to allow elements to totally redistribute in the solid.

Under these conditions, solidification can evolve to result in two opposite profiles. When an element partitions towards the liquid side of the S/L interface ($k < 1$), a compositional profile like the one in Figure 11 will result. A depleted liquid concentration will result for k larger than the unit (Figure 12). This difference in the segregation of different elements will give rise to different concentration profiles.

Bibliographical information [4, 11, 12] indicates that $k_{Ni} < 1$ and $k_{Cr} > 1$ in the Fe-Cr-Ni system (0.4 and 1.3 respectively when evaluated in primary ferritic alloys). Unfortunately, the Fe-Cr-Mn system is not as thoroughly studied as the Fe-Cr-Ni ternary. A lot of information, especially that regarding the details of the primary phase fields, is not available. This is where simulation tools could show their potential.

Free energy calculations based on Thermo-calc™ were used to define the partitioning coefficients for manganese and chromium. All simulations were done considering an alloy that contained 10.5 wt. % Cr, 0.048 wt. % C, 0.031 wt. % Si and manganese ranging from zero to twenty weight percent.

As Figure 13 presents, manganese concentration is always computed to be higher in the liquid, thus producing a partitioning coefficient less than one. These same simulations indicate that chromium has an apparent $k < 1$ for alloys with less than 10 weight percent manganese and $k > 1$ for richer alloys. This means that manganese and chromium should enrich the liquid phase during the solidification of alloys with less than 10 weight percent manganese. For alloys above that limit, manganese should enrich the liquid phase while chromium should be depleted from it.

According to the Thermo-calc™ simulations, Figure 11 represents the segregation profile for manganese at any composition, or for chromium in Mn-lean alloys. Figure 12 schematically represents the case of chromium at Mn-rich compositions. Even though the simu-

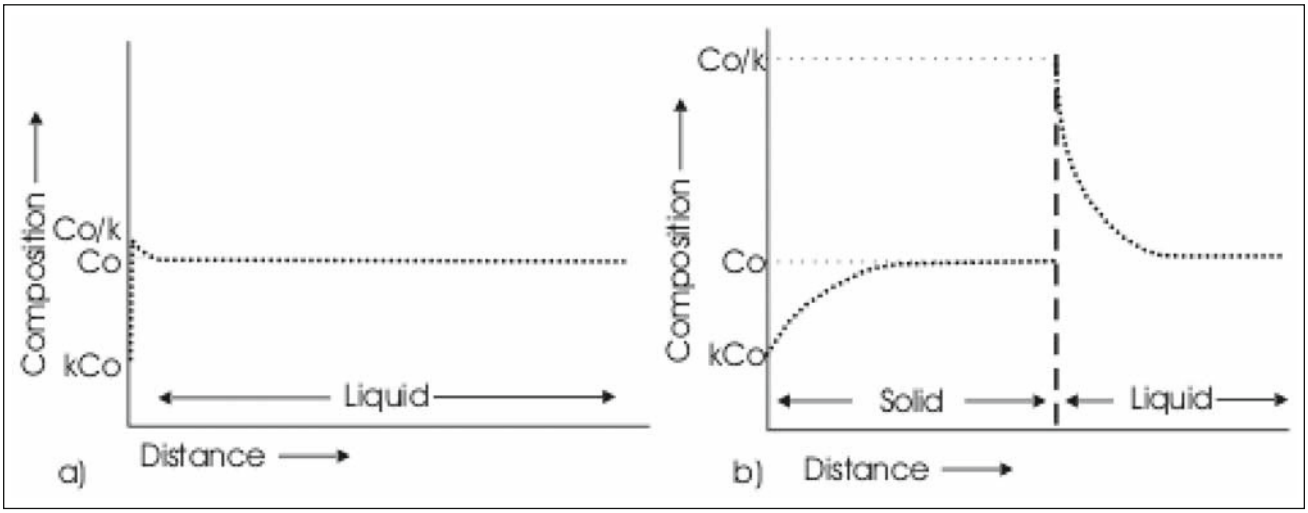

Figure 11 – Schematic representation of the k < 1 solidification of an alloy

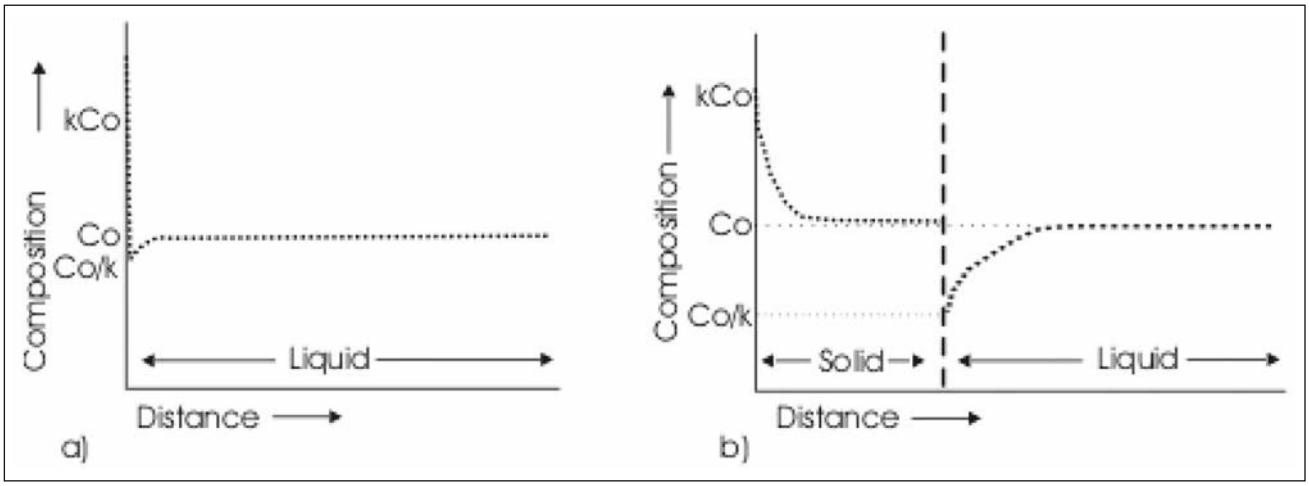

Figure 12 – Schematic representation of the k >1 solidification of an alloy

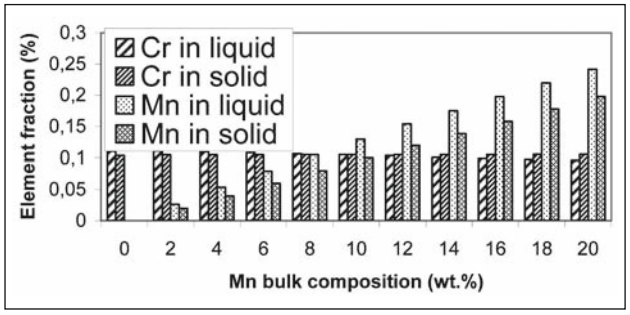

Figure 13 – Chromium and manganese fractions of the liquid and solid phase upon the solidification of Mn-based weld metals – Thermo-calc™ simulation

lations are not exact, they serve as a qualitative tool that could help to predict the segregation pattern.

With the relative magnitude of the partitioning coefficients (above or below the unit) for the three major alloying additions of this study available, and based on the previous discussion, a general mechanism for the segregation profile of these welds can be proposed. For the description of this mechanism, nickel and manganese can be treated similarly since both have a $k < 1$ along their whole compositional range when alloyed with iron.

Under normal welding conditions, the first solid to form will exhibit a Cr or Ni_{eq} compositional profile that is a function of the particular partitioning coefficient of the element. Simulations by Lippold and Savage [9] present clear distinctions between the segregation profile for Cr and Ni (Figure 14) in nickel-lean alloys, with lower chromium content and higher nickel content in the last liquid to solidify. As Cieslak *et al*. [10] proposed, this minimum and maximum are expected to occur at the solidification structure boundary.

EDS line scans indicate that indeed, for compositions leaner than ten weight percent, nickel concentration profile opposes that of chromium [Figure 15 a)]. The maximum nickel and minimum chromium occur at the region that was the last liquid to solidify. Conversely, the maximum chromium and minimum nickel concentrations are at the core of the solidification structure.

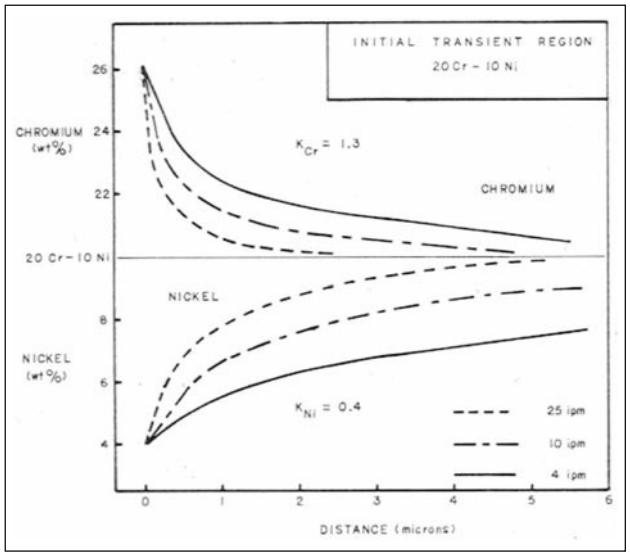

Figure 14 – Calculated chromium and nickel distribution in the initial transient region during solidification as delta ferrite at different cooling rates [9]

For the case of alloys with more than ten weight percent nickel, the observed profile was different [Figure 15 b)]. The nickel and chromium profiles were similar, having maxima and minima at the same points. In accordance with its partitioning ($k < 1$), nickel has its minimum at the structure core and its maximum at the region where the last liquid solidified. Although the chromium partitioning coefficient has not been reported to be smaller than one in these alloys, a detailed observation of the liquidus and solidus line at this composition level indicates that it is very close to one.

Further bibliographical review indicates that this type of profile has been found at similar ratios of chromium to nickel. Lippold [9], Cieslak [10] Suutala [13], and Takalo [14], have all found segregation profiles where chromium imitates the behaviour of nickel in alloys that were determined to be primary austenitic. The same researchers and Fredrikson [15] have also published profiles where the concentration of nickel opposes that of chromium for alloys that were found to be primary ferritic. None of them presented a thorough explanation

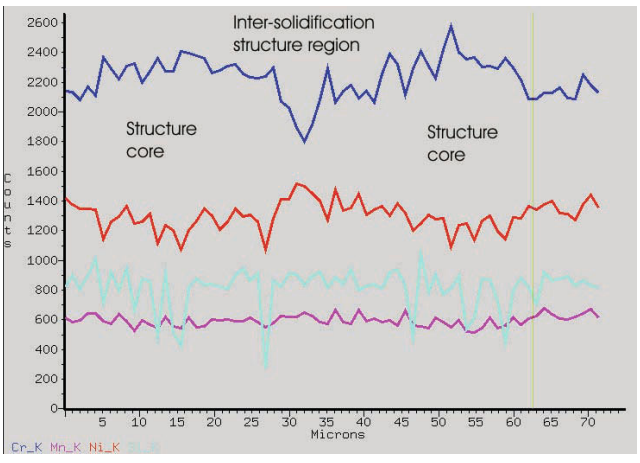

a) Ni1 segregation profiles

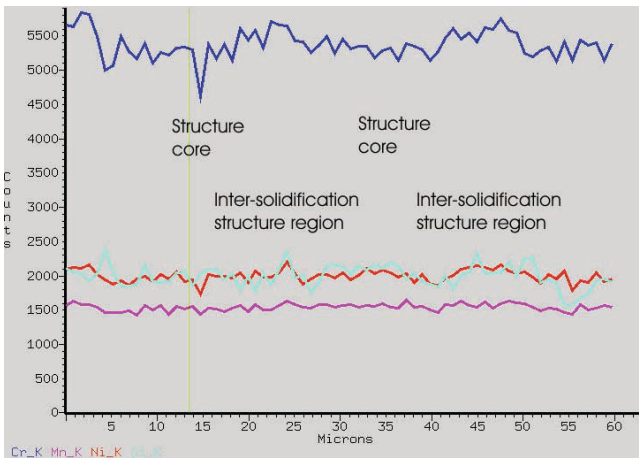

b) Ni3 segregation profiles

Figure 15 – Ni segregation profiles - EDS

for this discrepancy between the measured profiles and the expected profiles based on their partitioning in the primary austenitic alloys.

As the Thermo-calc™ simulations revealed, manganese behaves like nickel (k < 1) while chromium changed its segregation direction. Still, the partitioning of chromium was found to be opposite to what the computer simulations predicted (Figure 13). Chromium was rejected towards the liquid in alloys with more than ten weight percent manganese. In leaner alloys, chromium exhibited a partitioning coefficient greater than one. This behaviour exhibited by chromium is similar to the one predicted and observed for the case of rich Ni-based weld metals (Figure 14).

In Mn-based alloys with less than ten weight percent manganese, the segregation profile of chromium opposes that of manganese. In accordance with its predicted partitioning, the manganese content achieved a maximum at the solidification interface. In the same region, the chromium content reached a minimum for lean manganese alloys [Figure 16 a)]

For the case of alloys with manganese content above ten weight percent, chromium had its maximum at the region that solidified last. [Figure 16 b)]. Although manganese segregation was observed to be lower in these alloys, its maximum was at the same region as that for chromium. This result agreed with its predicted partitioning.

Supported by the segregation profiles, X-ray diffraction and metallographic analyses performed during this study, a comparison with previous work can be done. Cieslak [10] proposed a solidification pattern for chromium and nickel based on their observations of primary austenitic and ferritic weld metals. The present study verified these observations. The manganese behaviour for the different primary phases can also be included. Figure 17 presents the combined segregation patterns for primary ferritic and primary austenitic stainless steels.

Based on the segregation found in the weld metals of this study, it seems plausible that the differences between the measured and estimated M_S are related to segregation. The compositional gradient between the first and last solid to form is sufficient to result in different local transformation temperatures along the solidification structure. The final effects are a shift of the "bulk" transformation temperature to that determined by the composition of the first solid to form as well as a "gradual start" of the martensitic expansion instead of an abrupt one.

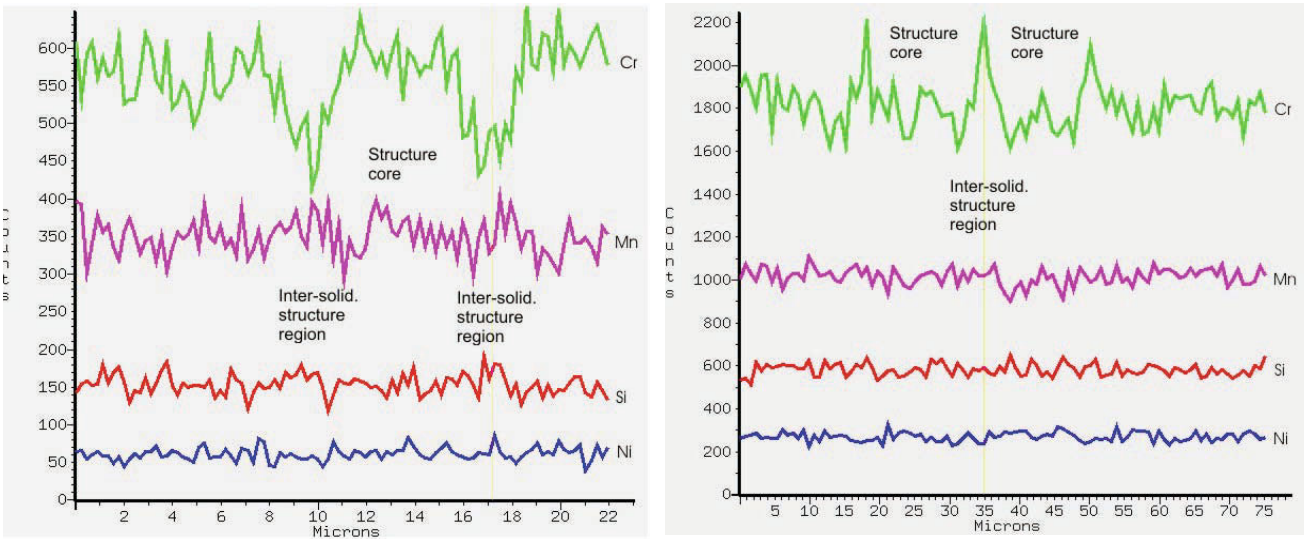

a) Mn5 segregation profiles **b) Mn6 segregation profiles**

Figure 16 – Mn segregation profiles - EDS

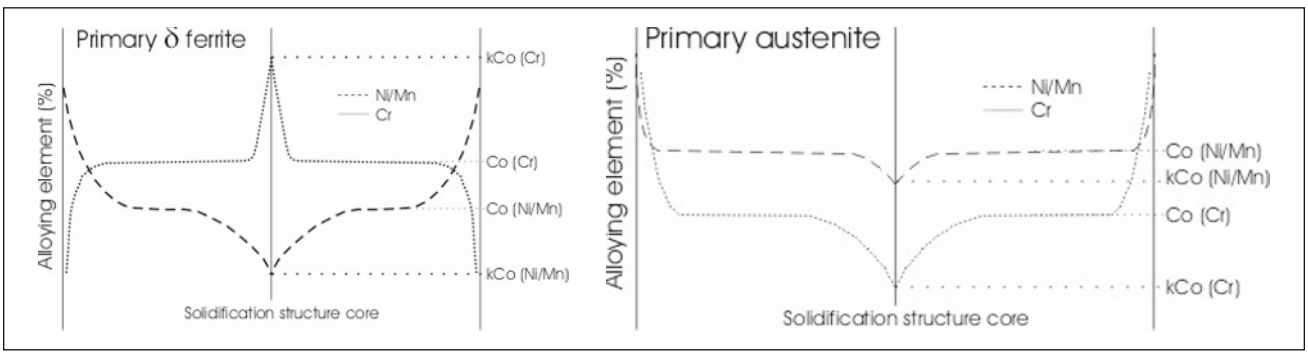

a) for primary ferritic weld metals **b) for primary austenitic weld metals**

Figure 17 – Segregation profiles found for chromium, manganese and nickel

This gradual start of the martensitic transformation can be clearly seen on Figure 2 where the slightly different local M_S along the solidification structure cause a gradual start of the expansion (in a strain vs. time analysis). If no segregation existed in the analyzed coupons, the start of the martensitic expansion would be a sharp change of curvature in the strain vs. time history instead of the evaluated curved one.

Although the last solid to form (the one in the inter-solidification structure region) may transform to martensite, its transformation might not even be detectable with standard measuring techniques. The fraction of this solid, in comparison to the fraction of the first solid to form is so small that its volumetric expansion will be barely noticeable. Furthermore, this last liquid to freeze will not transform to martensite in the presence of high concentrations of austenite- or ferrite-stabilizers. If that is the case, the last solid to form will remain as retained austenite or δ-ferrite.

From this segregation study, the positive inflexion points in the transformation temperature trends can also be explained (see Figure 9, 6.5 wt. % Ni and Figure 10, 9.5 wt. % Mn). Chromium segregation is high enough to explain the differences in the evaluated and predicted M_S temperatures. However, since the behaviour of chromium changes according to the primary phase, a different segregation pattern will result. Thus, modifications to the transformation temperature trend will result according to the concentration of chromium in the first solid to form.

Chromium enriches the solid (as its partitioning coefficient dictates) in alloys leaner than 6.5 weight percent nickel and 9.5 weight percent manganese. This enrichment will effectively cooperate with other alloying additions by reducing the martensite start temperature. Therefore, the change in the M_S will increase as the alloying increases.

For richer alloys, the partitioning coefficient for chromium approaches one, and the chromium solubility controls the segregation process. Austenite is the first solid to form in these alloys. Since chromium atoms (bcc) are not compatible with the austenitic matrix (fcc) chromium is rejected to the liquid phase. This rejection explains the higher chromium concentration in the last solid formed in Mn- and Ni-based primary austenitic weld metals.

As in the case of the leaner alloys, chromium helps reduce the M_S temperature. Because in this case it enriches the liquid, its effect in reducing the transformation temperature is diminished, and the slope of the M_S vs. bulk alloy curve is reduced.

3.4 Solidification mode differences

Inspection of metallographic samples attacked with the Primary Solidification Structure etchant (PSS solution, Table 2) revealed differences in the solidification structure of several alloys. It was observed that alloys identified as primary ferritic always presented a dendritic solidification mode. In the alloys identified as primary austenitic, the observed solidification mode was cellular.

This observation matches those made by Hultgren [4], Suutala [13], Takalo [14], and Fredriksson [15]. Primary ferritic stainless steels that solidify at high rates typical of welding processes will do so in a dendritic mode [Figure 18 a) and Figure 19 a)]. At these solidification rates, primary austenitic stainless steels will solidify in a cellular mode [Figure 18 b) and Figure 19 b)].

This cellular solidification breakdown seems to be influenced by the partitioning of elements. Pseudo-binary phase diagrams indicate that the partitioning of nickel should be noticeably higher in ferritic compositions than in austenitic compositions [11]. Segregation profiles like those of Figure 15 indicate that indeed, a higher content of nickel is present in the interdendritic region for primary ferritic compositions.

This higher partitioning of nickel towards the liquid phase can increase the thermodynamic undercooling, thus making cellular solidification unstable. Secondary

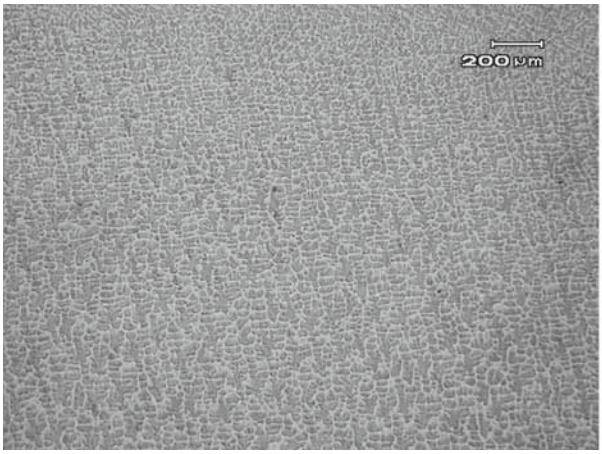

a) Ni2 solidification structures
Primary ferritic

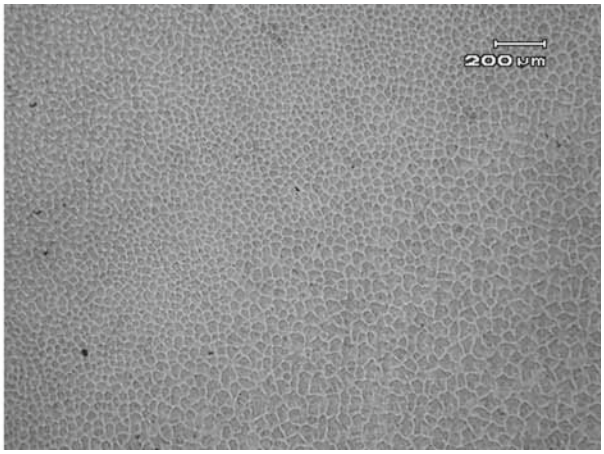

b) Ni3 solidification structures
Primary austenitic

Optical microscopy. PSS etchant, 10 seconds.

Figure 18 – Ni solidification structures

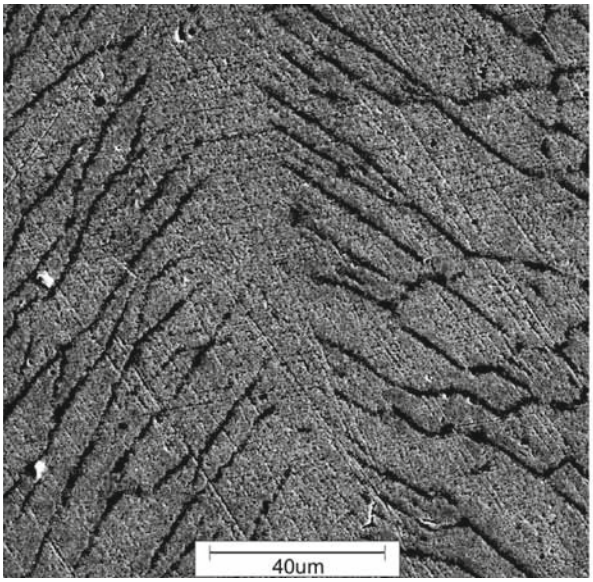

a) Mn5 solidification structures Primary ferritic (40 μm marker)

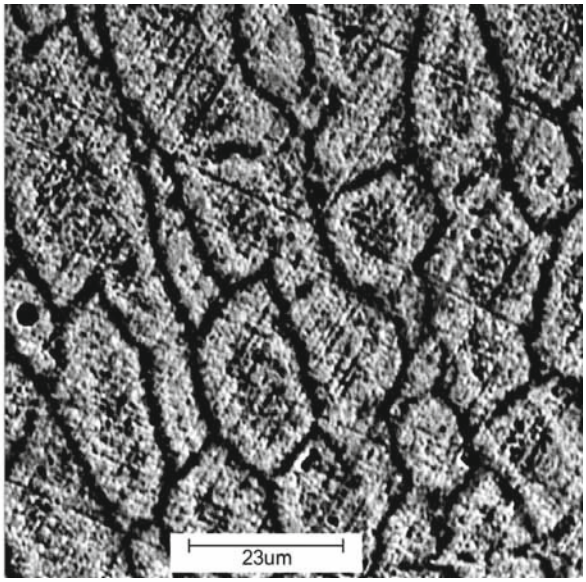

b) Mn6 solidification structures Primary austenitic (23 μm marker)

Scanning electron microscopy. PSS etchant, 30 seconds.

Figure 19 – Mn solidification structures

arms will appear, caused by the undercooling increment behind the dendrite tips.

Segregation profiles of the Mn-based alloys (Figure 16) do not indicate a level of partitioning as noticeable as in the case of the Ni-based alloys. Still, increased segregation of manganese into the liquid in the primary ferritic alloys is present. There was no evidence that this solute build-up was insufficient to destabilize the cellular growth.

The described differences in the solidification mode have served as an identification variable in previous primary-phase assessment studies [16-18]. The results from this study can be added to those of the previous studies to create an expanded alloying boundary between primary ferritic and primary austenitic weld metals.

3.5 A compositional boundary between primary ferritic and austenitic weld metals

Extensive work in this area has been done in previous studies [4, 13, 14, 16, 17, 18, 21, 22]. However, most of this earlier work focussed on welding alloys with high concentrations of chromium and either high or low nickel content. No work has been published for high manganese compositions, or at intermediate levels of nickel. Since most of the commercially important stainless steel welding alloys are of high chromium content, little work has been developed at leaner compositions.

By means of direct sample inspection, many authors have proposed a compositional boundary between weld metal compositions that solidify as primary ferrite or austenite. The criteria they used range from the detection of retained phases and primary solidification structure to the evaluation of cracking susceptibility. All of those researchers published their boundary as a Cr_{eq}/Ni_{eq} ratio.

The use of a ratio of stabilizer elements as definition of the phase boundary resides in the fact that the presence of a particular element alone does not dictate the primary phase. The balance of the elements that stabilizes different phases will dictate the formation of a particular primary phase.

Because no single alloying theory can predict the effect of all the alloying additions to steel, predictions of primary phase formation has been done mainly by experimental observation. The complexity of the different processes that occur during solidification and the transitory nature of many of the involved elements limit the use of any theoretical approach.

Suutala [13] proposed that Cr_{eq}/Ni_{eq}~1.52 should define the primary phase boundary for weld metals. Lower ratios were proposed for the case of processes where the growth rate of the solid phase was slower, and reduced thermal gradient or nucleation effects [13] were suggested as potential causes.

Although the chromium content in this study is below that of Suutala *et al*., the results from the current Ni-based weld metals are in accordance with their proposal. Weld metals with chromium-to-nickel ratios under 1.52 solidified as primary austenite. X-ray diffraction analyses as well as metallographic inspection revealed the presence of retained austenite in the core of the primary solidification structure and the total absence of δ-ferrite (Figure 20).

Alloys Ni1 and Ni2 have Cr/Ni ratios of 3.2 and 1.8, respectively. Their higher fraction of ferrite stabilizers promoted the formation of ferrite as their primary phase. In addition to the total absence of austenite in these compositions (Figure 20), both of them solidified

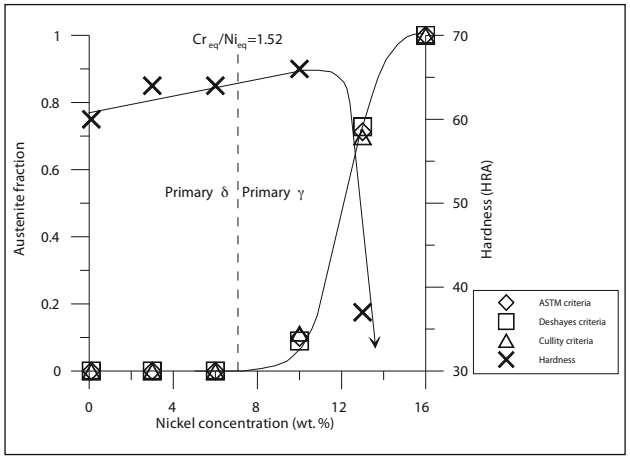

Figure 20 – Primary phase boundary of the Ni-based weld metals on the austenite quantification (XRD) and hardness

in a dendritic mode. This solidification mode has also been used by many authors as evidence of the primary phase to form (see previous section).

Although Suutala proposed an equivalency of nickel to manganese of one-half (e.g. Ni_{eq} = Ni+0.5Mn+…) the results from this study suggest a different equivalent. According to Suutala's conversion, the Mn6 (11.2Cr12.8Mn0.30Si) alloy would have Cr_{eq}/Ni_{eq} = 1.80, which would mean a primary ferrite solidification in a dendritic mode. Metallographic observation of this composition [Figure 19 b)] reveals that it not only solidifies in a cellular mode like the primary austenitic Ni-based weld metals [Figure 18 b)], but that it also presents a segregation profile typical of primary austenitic weld metals (Figure 16), where chromium is rejected to the liquid during the formation of the first solid.

A less conservative conversion of sixty percent of manganese to nickel (e.g. Ni_{eq} = Ni+0.6Mn+…) would locate this composition inside the already verified ratio of chromium-to-nickel equivalents that predicts primary austenitic weld metals. The information presented in Figure 21 also serves to verify the proposed conversion between manganese and nickel.

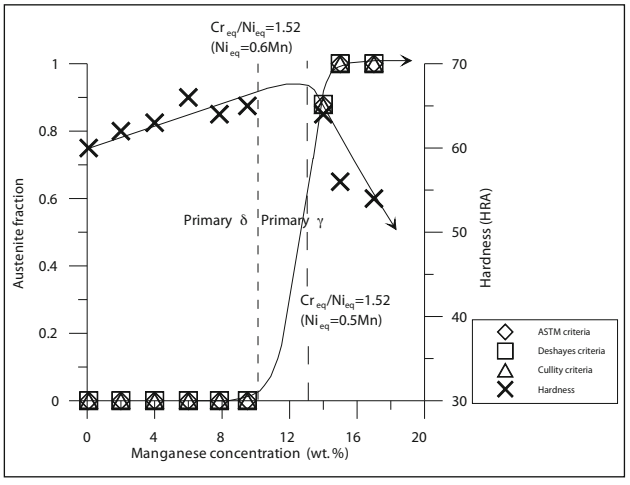

Figure 21 – Primary phase boundary of the Mn-based weld metals on the austenite quantification (XRD) and hardness

This change in the equivalency of nickel to manganese follows a bigger trend. Several authors have attempted to quantify the potency of manganese regarding austenite stabilization relative to that of nickel in the context of solidification. Based on their observations, different equivalents have been proposed. Figure 22 presents some of these equivalents plotted against the maximum content of manganese in their particular experimental matrices. As Figure 22 reveals, the higher the manganese content in the analyzed matrix, the higher the effect of manganese on stabilizing austenite.

At the same time, Curve A of this figure exhibits a slope change around four weight percent manganese. This change in the ability of manganese to stabilize austenite can also be observed in its capability to reduce the M_S (see Figure 10).

While the complex behaviour of manganese in alloying is clearly not well understood, its effects are important in welding alloys. Although the focus of this study is not the differences in manganese behaviour, this phenomenon is noticed in an effort to settle a precedent for further studies.

The points in Curve B of Figure 22 correspond to experimental matrices that contained substantial amounts of other ferrite stabilizer elements. The trend they follow is similar to that of experimental matrices containing significantly less ferrite stabilizers.

As demonstrated in this section, modifying the manganese-to-nickel equivalency resulted in a compositional limit that more clearly separates the primary phases, including alloying contents well outside those of commercial interests.

Figure 23 presents the compositional limits proposed by several authors plotted against the maximum austenite stabilizer content of their research matrices. This is a way of presenting the maximum compositional reach of their conclusions.

As the trend in this figure presents, a Cr_{eq} to Ni_{eq} ratio of 1.52 separates the primary phases in weld metals for a wide range of compositions. The effects of chromium, silicon, manganese, and nickel are considered in this ratio. Weld metals with ratios above 1.52 are expected to solidify as δ-ferrite in a dendritic mode. Primary

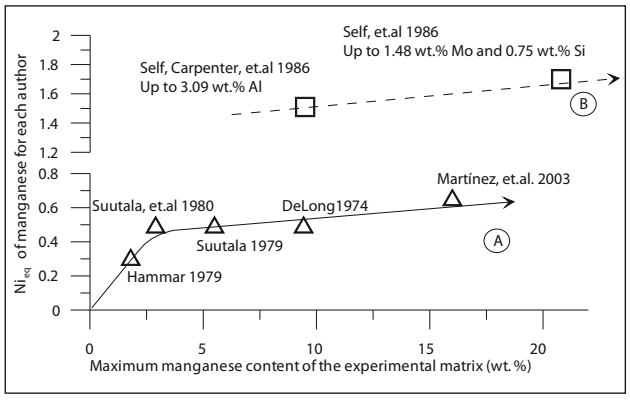

Figure 22 – Nickel equivalences of manganese for experimental matrices of different manganese contents

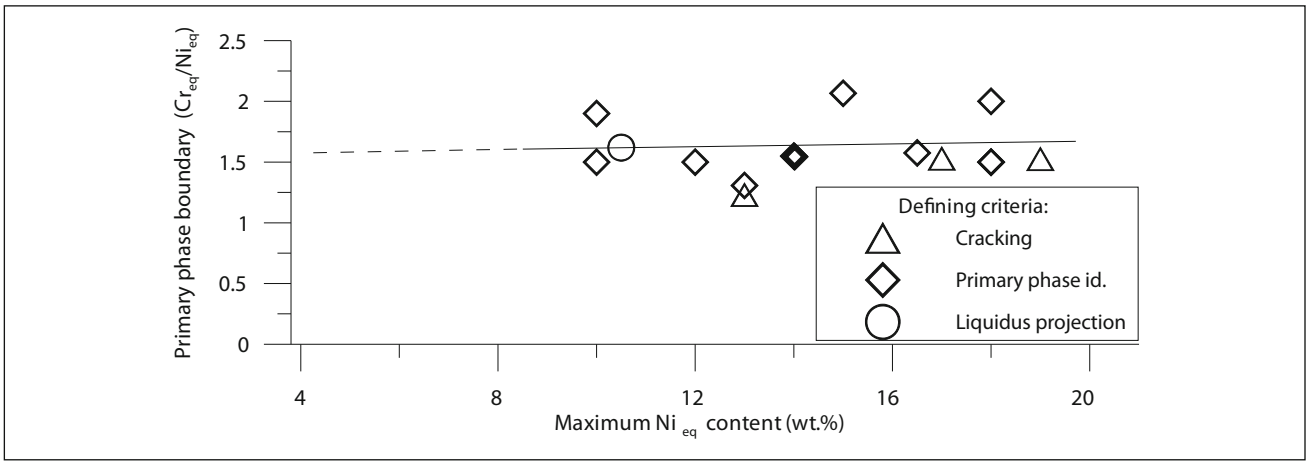

A bold diamond represents the findings of this study.

Figure 23 – Compositional boundary between primary austenitic and ferritic alloys for different authors

austenite solidifying in a cellular mode is expected for weld metals with ratios below 1.52. The findings of this research, represented by a bold diamond symbol, show excellent agreement with the literature data.

3.6 Weldment morphology modification by means of silicon additions

Successful development of a compressive residual stress at the weld toe does not depend only on the martensitic transformation. If stress concentrators are present, the effect of the phase transformation can be negated.

The Ni-based weld metals developed during this study exhibited adequate fluidity and resulted in morphologies that are acceptable for this project. Unfortunately, the Mn-based weld metals exhibited a more irregular morphology. Alloys containing more than seven weight percent manganese resulted in beads so distorted that stress concentration points were inevitable.

In an effort to enhance the fluidity of the Mn-based weld metals, a complete welding-parameter investigation study was conducted. By carefully increasing the heat input, a higher weld pool temperature was achieved. Fine tuning variables like voltage and current also helped to obtain weld beads with much better morphology. However, the increase in current required to raise the temperature of the molten metal also resulted in undercutting which acts as a local decrease of the weld toe radius, thus increasing the SCF over 10 times [20]. Thus, adjustment of welding parameters alone resulted in an incomplete solution to the weld morphology problem.

Silicon additions are known to increase the fluidity of many molten metals. As the Si-Fe-Mn ternary diagram depicts [11], the addition of silicon lowers the melting temperature, which will lead to an increase in the fluidity of the molten metal given the same heat input.

However, silicon additions have more impact in the weld metals. The presence of higher silicon content can favour the formation of a slag system, which provides cover for the molten metal during welding, reducing heat removal from the weld pool. Consequently a more fluid weld metal results.

At the compositional range evaluated (0.30 to 1.88 weight percent), silicon showed no evidence of altering the martensitic transformation. Metallographic and XRD analyses revealed no change in the final martensite fraction, which remained over 95 percent volume for all of the compositions. Hardness measurements indicate little influence of silicon on the martensitic transformation (Figure 24).

From bead-on-plate (BOP) coupons it was found that high silicon additions were not necessary to improve the fluidity of the weld metals (see Figure 25). A 0.4-wt % Si addition was enough to improve the fluidity so that a smooth weld surface and a good wet angle resulted (see Figure 26). Although alloys with silicon contents over 0.6 weight percent manifested an even smaller wetting angle, the weld contour and surface was not any better than those of the leaner alloys.

With the morphology problem solved, the composition of a weld metal that would result in a high level of compression at the toe was devised. This weld metal should start its transformation at the lowest possible temperature below 450 °C, temperature evaluated as

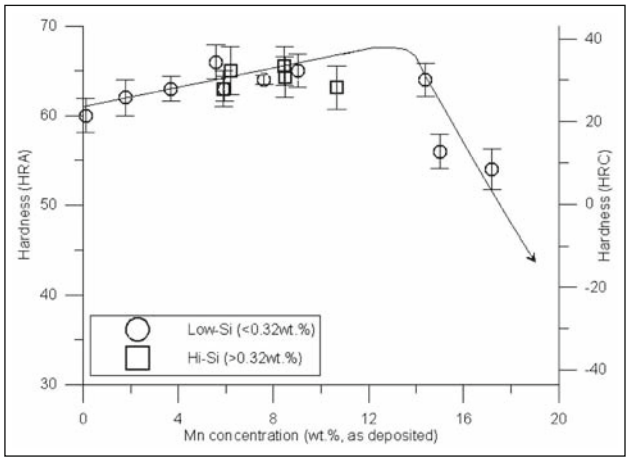

Figure 24 – Comparison between the hardness of high and low silicon weld metals

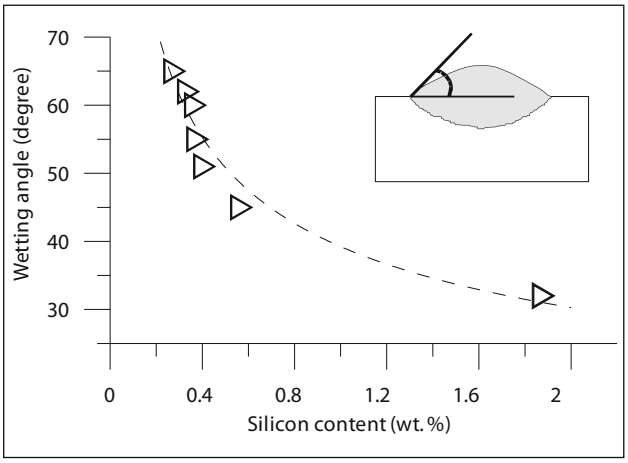

Figure 25 – Effect of silicon additions on the resulting weld geometry (BOP coupons)

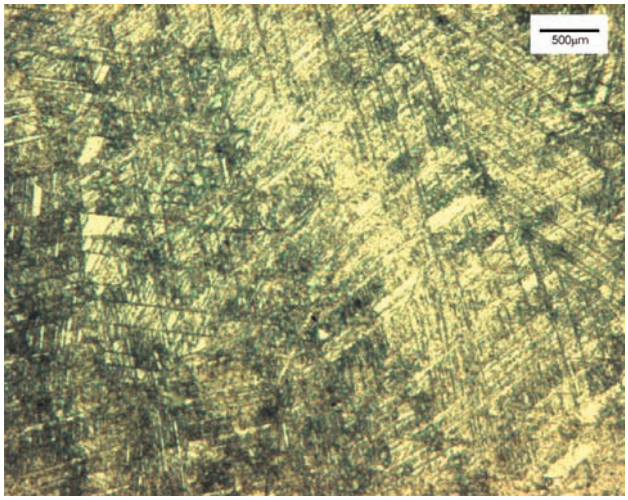

FS etchant (30 s). Martensite plus austenite.

Figure 27 – Best effort weld metal

the maximum M_S at which the thermal contraction effect could not negate the martensitic transformation [8, 19]. At the same time, the best effort weld metal should finish its transformation well above room temperature and contain enough silicon to result in acceptable weld morphology.

3.7 The residual stress field around the weld toe

A final weld metal composition based on manganese, chromium and silicon was selected for final residual stress testing. As mentioned in the beginning of this document, the selection of manganese over nickel for the development of this weld metal was based on cost considerations.

This best effort weld metal satisfies all the requirements presented in previous parts of this document. The thermal contraction effect is minimized since this alloy starts to transform to martensite just below 200 °C. Furthermore, the transformation ends well above room temperature (over 100 °C), insuring the maximum possible formation of martensite. Metallographic and XRD analyses indicate that this composition results in over ninety percent volume martensite with some traces of ferrite, its primary phase (Figure 27).

Proper weld profile was ensured by means of welding parameter optimization and silicon additions.

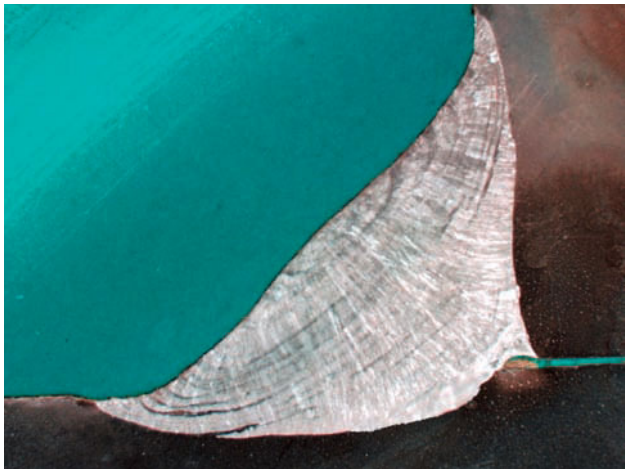

Figure 28 – Best effort weld metal transversal view

(Figure 28). No visible defect, including undercut, inclusion, crack, porosity, was found in any sample.

As expected, a high compressive residual stress was found in the region adjacent to the weld toe. Its level dropped from the maximum at the weld toe, both on the horizontal plane [Figure 29 a)] as well as in the vertical plane under the weld toe [Figure 29 b)]. The compressive stress field extended to 0.95 millimetres under the surface. Surface level measurements at 25 millimetres from the weld toe still indicate compression.

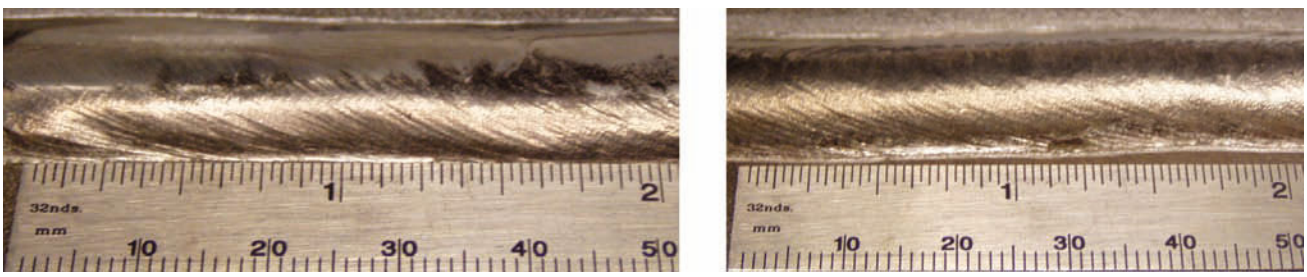

a) Si3 weld metals **b) Si4 weld metals**

Similar heat inputs.

Figure 26 – Bead-on-plate

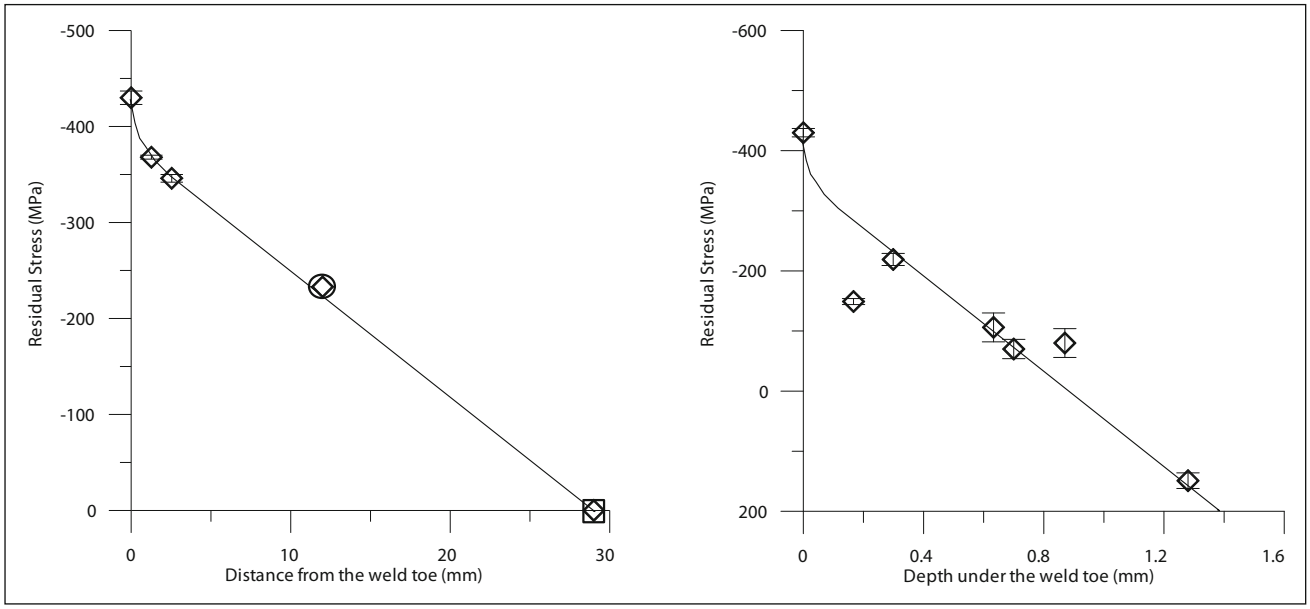

a) at the surface level **b) underneath the surface level**

Best effort weld metal. X-ray diffraction measurements.

Figure 29 – Residual stress profile measured from the weld toe

Additional samples with higher transformation temperatures were subjected to residual stress mapping by means of XRD. As expected, a correlation between the transformation start temperature and the maximum residual stress was found (Figure 30). The lower the martensite start temperature, the higher the magnitude of the compressive stress.

In summary, by controlling the martensitic transformation, a high compressive residual stress field was induced at the weld toe. This residual stress field of -430 MPa is expected to increase the fatigue life of the welded components. Actual verification of this increase in fatigue life will be relegated to future studies.

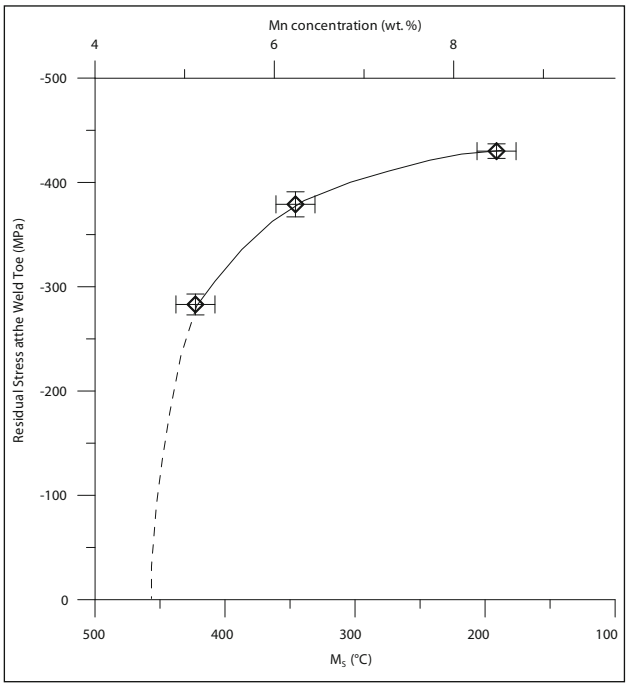

Mn-based weld metals. XRD.

Figure 30 – Transversal residual stress measurements taken at the weld toe

4 CONCLUSIONS

A methodology that altered weld metal composition for the purpose of creating a compressive residual stress field in plain-carbon steel structural weld toes was established. Maximum martensite fraction and hardness were achieved from the 10Cr-10Ni and 10Cr-14Mn compositions. Alloys with higher contents of nickel or manganese resulted in retained austenite.

Segregation of chromium, nickel, and manganese are responsible for the encountered differences between evaluated and predicted M_S temperatures. The differences are not systematic and are related to the partitioning behaviour these elements manifest for different steel phases.

Within the range of weld solidification rates, primary austenitic compositions solidify as cells while primary ferritic solidifies as dendrites. In weld metals, primary austenite forms when Cr_{eq} to Ni_{eq} ratios are less than 1.52, while primary ferrite forms at higher ratios. Within the range of compositions of this study, the conversion for the manganese effect to nickel is 0.6 (e.g. Ni_{eq} = 0.6 Mn). This conversion should be expected to increase slightly as the manganese content is raised. The δ/γ boundary (Cr_{eq}/Ni_{eq} = 1.52) does not seem to be altered by changes in the γ stabilizer content.

Silicon additions and modifications to welding parameters can alter the morphology of weld beads. As little as 0.4-wt %-Si addition will noticeably improve the bead morphology of Mn-Cr-based gas metal arc welds in steel.

A Mn-Cr-Si weld alloy that induces a 430 MPa compressive stress field at the weld toe by means of martensitic transformation has been developed. This compressive stress field is maximum at the weld toe.

ACKNOWLEDGEMENTS

The author would like to thank his advisors Prof. Glen Edwards and Prof. Stephen Liu for the patient guidance and great support in the conduction of the present study. He also would like to thank Caterpillar Inc. for the financial support for the conduction of the research program.

REFERENCES

[1] Davies G.J.: Perfomance in service, Essential Metallurgy for Engineers, London: Van Nostrand Reinhold, 1985.

[2] Ohta A., Watanabe O., Matsuoka K., Maeda Y., Suzuki N., Kubo T.: Fatigue strength improvement of box weld by low transformation temperature welding wire and PWHT, IIW Document No. XIII-1758-99, 1999.

[3] Ohta A., Watanabe O., Matsuoka K., Maeda Y., Suzuki N., Kubo T.: Fatigue strength improvement of box weld by low transformation temperature welding wire, IIW Document No. XIII-1759-99, 1999.

[4] Hultgren A.: Phenomena in 1.10 per cent. Carbon Steel Ingots, J. Iron and Steel Institute, 1929, Vol. 70, pp. 69-113.

[5] Cullity B.D.: Elements of X-Ray diffraction, 2nd Ed, USA: Addison-Wesley Pub. Co. Inc., 1978.

[6] Self J.A., Carpenter B.F., Olson D.L., Matlock D.K.: Phase transformations and alloy stability in Fe-Mn-Ni-Cr-Al weld metal, Alternate Alloying for Environmental Resistance Worrenville: AIME-TMS, 1986.

[7] Self J.A., Olson D.L., Edwards G.R.: The stability of austenitic weld metal, Presented at the International Cryogenic Materials Conference (ICMC), “Cryogenic Materials and Their Welding”, Kiev USSR, July 24-26 1984.

[8] Martinez F.: Development of compressive residual stress in structural steel weld toes by means of weld metal phase transformations, Doctoral Thesis, Colorado School of Mines, 2004.

[9] Lippold J.C., Savage W.F.: Solidification of austenitic stainless steel weldments: Part I- A Proposed Mechanism, Welding Journal, 1979, Vol. 58, 12, pp. 362s-374s.

[10] Cieslak M.J., Ritter A.M., Savage W.F.: Solidification cracking and analytical electron microscopy of austenitic stainless steel weld metals, Welding Journal, 1982, Vol. 61, 1, pp. 1s-8s.

[11] Raghavan V.: Phase diagrams of ternary iron alloys, Metals Park OH: ASM International, 1987.

[12] Flemings M.C.: Solidification processing, USA: McGraw-Hill, 1974.

[13] Suutala N.: Effect of Manganese and nitrogen on the solidification mode in austenitic stainless steel welds, Metallurgical Transactions A., 1982, Vol. 13A, pp. 2121-2130.

[14] Takalo T., Suutala N., Moisio T.: Austenitic Solidification mode in austenitic stainless steels, Metallurgical Transactions A., 1979, Vol. 10, pp. 1173-1181.

[15] Fredriksson H.: The solidification sequence in an 19-8 stainless steel, investigated by directional solidification, Metallurgical Transactions, 1972, Vol. 3, pp. 2989-2997.

[16] Takalo T., Suutala N., Moisio T.: Influence of ferrite content on its morphology in some austenitic weld metals, Metallurgical Transactions A., 1976, Vol. 7A, pp. 1591-1592.

[17 Suutala N., Takalo T., Moisio T.: Ferritic-austenitic solidification mode in austenitic stainless steel welds, Metallurgical Transactions A., 1980, Vol. 11A, pp. 717-725.

[18] Suutala N.: Effect of solidification conditions on the solidification mode in austenitic stainless steels, Metallurgical Transactions A., 1983, Vol. 14A, pp. 191-197.

[19] Tominaga T., Miki C.: Effect of steel strength and Ms temperature on fatigue performance of low temperature transformation electrode, IIW Document No. XIII-1953-02, 2002.

[20] Brennan F.P., Peleties P., Hellier A.K.: Predicting weld toe stress concentration factors for T and skewed T-joint plate connections, Int. J. of Fatigue, 2000, Vol. 22, pp. 573-584.

[21] Takalo T., Suutala N., Moisio T.: The relationship between solidification and microstructure in austenitic and austenitic-ferritic stainless steel welds, Metallurgical Transactions A., 1979, Vol. 10A, pp. 512-514.

[22] Brooks J.A.: Solidification and solid state transformations of austenitic stainless steel welds, in the Proceedings of the Trends in Welding Research in the United States, ASM, New Orleans, Louisiana, November 16-18 1981.